Research article

Hong Zheng[a], Bingkun Chen[a,]*, Lifu Shi, Fa Zhang, Ziheng Zhao, Yue Liu, Lingling Huang, Bingsuo Zou* and Yongtian Wang*

Stable blue-emissive aluminum acetylacetonate nanocrystals with high quantum yield of over 80% and embedded in polymer matrix for remote UV-pumped white light–emitting diodes

https://doi.org/10.1515/nanoph-2020-0142
Received February 24, 2020; revised March 15, 2020; accepted March 16, 2020

Abstract: Blue-emissive nanocrystals (NCs) with high photoluminescence quantum yields (PL QYs) and excellent stability are essential for lighting and displays. Here, a facile top-down approach (including two steps: thermal annealing and ultrasonic treatment) by using aluminum acetylacetonate ($Al(acac)_3$) as a precursor is adopted to fabricate blue-emissive $Al(acac)_3$ NCs with high PL QY reaching 81.8%, the highest reported value for the aluminum compound-based NCs so far. Additionally, the as-fabricated $Al(acac)_3$ NC solution (in toluene) exhibits high stability under air atmosphere condition, maintaining 61.2% of initial PL QY after 1 year. Furthermore, solution-processed $Al(acac)_3$ NCs/poly(methyl methacrylate) (PMMA) composite film with blue emission is demonstrated. Finally, combinations of the blue-emitting $Al(acac)_3$ NCs/PMMA composite film with red-emitting and green-emitting $CuInS_2$ composite films are realized, resulting in remote ultraviolet-pumped white light-emitting diodes with a high color rendering index of 91. These findings inform new blue-emissive NCs and composite films, potentially paving the way to design new structures of lighting and display devices.

Keywords: $Al(acac)_3$ nanocrystals; top-down approach; $Al(acac)_3$ NCs/PMMA composite film; remote UV-WLEDs.

1 Introduction

Phosphor-converted white light-emitting diodes (pc-WLEDs) have been indispensable sources in lighting industry and display systems due to their energy savings, environment-friendliness, and long persistence [1–5]. However, the traditional device structure is facing some problems to be solved as follows: (i) the working temperature of blue LED chips could reach 100°C to 150°C, which causes phosphors thermal degradation problem; (ii) the direct mixing of different-color phosphors is adopted to get high-quality white light, but the reabsorption of phosphors is severe; (iii) the potential blue light retinal injury of blue chip to human eyes [6, 7]. In respect to the aforementioned issues, remote ultraviolet-pumped WLEDs (UV-WLEDs) have received great attention [8–10]. This type of WLEDs not only can reduce the thermal degradation and reabsorption of phosphors, but also decrease the potential blue light hazard. The developments of remote UV-WLEDs put forward new requirements for blue-emitting materials and their composite films, which can be efficiently excited by UV light. However, most of commercial blue rare-earth phosphors with micrometer size cause easy aggregation and poor compatibility with polymers or optical glass matrix. Interestingly, blue-emitting NCs possessing

[a]**Hong Zheng and Bingkun Chen:** These authors contributed equally to this work.
***Corresponding authors: Bingkun Chen,** Beijing Engineering Research Center of Mixed Reality and Advanced Display, School of Optics and Photonics, Beijing Institute of Technology, Beijing 100081, People's Republic of China, e-mail: chenbk@bit.edu.cn. https://orcid.org/0000-0003-3714-166X; **Bingsuo Zou,** Beijing Key Laboratory of Nanophotonics and Ultrafine Optoelectronic Systems, School of Physics, Beijing Institute of Technology, Beijing 100081, People's Republic of China, e-mail: zoubs@bit.edu.cn; and **Yongtian Wang,** Beijing Engineering Research Center of Mixed Reality and Advanced Display, School of Optics and Photonics, Beijing Institute of Technology, Beijing 100081, People's Republic of China; and AICFVE of Beijing Film Academy, Beijing 100088, People's Republic of China, e-mail: wyt@bit.edu.cn
Hong Zheng: Beijing Key Laboratory of Nanophotonics and Ultrafine Optoelectronic Systems, School of Physics, Beijing Institute of Technology, Beijing 100081, People's Republic of China
Lifu Shi: Beijing Key Laboratory of Nanophotonics and Ultrafine Optoelectronic Systems, School of Materials Science and Engineering, Beijing Institute of Technology, Beijing 100081, People's Republic of China
Fa Zhang, Ziheng Zhao, Yue Liu and Lingling Huang: Beijing Engineering Research Center of Mixed Reality and Advanced Display, School of Optics and Photonics, Beijing Institute of Technology, Beijing 100081, People's Republic of China. https://orcid.org/0000-0002-3647-2128 (L. Huang)

outstanding solubility and compatibility with polymers are promising candidates for remote UV-WLEDs [11–14].

Although impressive progresses have been made in fabrication of blue-emitting NCs, such as remarkable CdSe [15–18], InP [19, 20], perovskites (e.g. $CH_3NH_3PbCl_3$, $CsPbBr_3$) [21–27], sulfur dots [28], silicon dots [29], and carbon dots [30], which still lag behind in efficiency and stability for LED applications [31, 32], it is much more important to develop new promising blue-emitting NCs. Aluminum hybrid compound counterparts have advantages of being inexpensive, nontoxic, and earth-abundant, which have aroused intense interests for researchers in the past several years [33–35]. Bai et al. [33] reported a blue-emissive boehmite (γ-AlOOH) hybrid nanoplates achieving photoluminescence (PL) quantum yield (QY) of 58%. In our recent previous works, we developed blue-emitting aluminum hydroxide (PL QY, 69%) with broad PL spectrum by using a single precursor decomposition method [34, 35]. Unfortunately, they exhibit poor solubility in solution and unsatisfactory compatibility with polymers, thus showing not suitable for using in remote UV-WLEDs.

Herein, we fabricated blue-emitting aluminum acetylacetonate [$Al(acac)_3$] NCs for the first time by using a facile top-down approach with $Al(acac)_3$ as a precursor, which contain two steps including (i) thermal annealing aiming to improve the crystallinity of the raw material and (ii) ultrasonic treatment to disintegrate the high crystalline precursor. The obtained $Al(acac)_3$ NCs exhibit multiple-peak emission spectrum behavior and high absolute PL QY reaching 81.8%. As far as we know, this is the highest reported PL QY value for the aluminum hybrid compound–based NCs so far [36]. We further fabricated transparent $Al(acac)_3$ NCs/poly(methyl methacrylate) (PMMA) composite film through roller coating with mixed solution of $Al(acac)_3$ NCs/toluene and PMMA/chloroform. Moreover, combinations of the blue-emitting $Al(acac)_3$ NCs/PMMA composition film with red- and green-emitting $CuInS_2$ composite films result in remote UV-WLEDs with a high color rendering index (CRI) of 91.

2 Experimental section

2.1 Materials

Aluminum acetylacetonate (99%; J&K Scientific Ltd., Beijing, China), PMMA (average molecular weight ~300,000; Alfa Aesar, Lancashire, United Kingdom), toluene, and chloroform (analytical grade; Beijing Chemical Reagent Co., Ltd., Beijing, China). All chemicals were used as received without further purification.

2.2 Fabrication of $Al(acac)_3$ NCs

The $Al(acac)_3$ precursor (1.625 g) was firstly dehydrated for 12 h under vacuum at 70°C, loaded into a quartz boat and then placed in the central region of a quartz tube in a furnace chamber. Before the heating process, high-purity inert gas (N_2) flowed through the quartz tube at a rate of 30 sccm for 30 min to eliminate the air. After 90 min of thermal annealing at 200°C under a 10 sccm constant N_2 atmosphere, the furnace was cooled to room temperature, and the product was collected. The resulting sample after thermal annealing is denoted as S1. The product was dissolved in toluene with concentration of 0.1625 g mL^{-1}, and the $Al(acac)_3$ NCs was obtained by subsequent ultrasonication (6 h), which was denoted as S2. Powdered S2 was realized by using vacuum drying at 70°C.

2.3 Fabrication of $Al(acac)_3$ NCs/PMMA composite film

The fabrication of $Al(acac)_3$ NCs/PMMA composite film includes three stages. Stage I: 0.825 g S2 powder was dispersed in 1 mL toluene, and then the solution was mixed with PMMA chloroform solution (0.5 g ml^{-1}) under stirring; subsequently, the mixed solution was dropped onto the surface of a glass substrate. Stage II: the mixed solution was flattened with a glass rod. Stage III: the wet film was placed in a ventilated place for natural volatilization of the solvent to obtain a dry transparent film. We prepared red- and green-emitting $CuInS_2$/PMMA composite films by using the same method.

2.4 Fabrication of remote UV-LED

The monochrome blue-emitting remote UV-LED was realized through the process that the $Al(acac)_3$ NCs/PMMA film was put on the top of UV-LED chip (370 nm) encapsulated with silicone resin. Remote UV-WLEDs were fabricated by stacking the three color-converting films of red-emitting, green-emitting $CuInS_2$ NCs/PMMA, and $Al(acac)_3$ NCs/PMMA on the top of UV-LED chip in sequence from the bottom to up.

2.5 Characterizations

Ultraviolet-visible (UV-vis) absorption spectra were measured on a V-570 spectrophotometer. Photoluminescence spectra were collected on a F-380 fluorescence spectrometer. Scanning electron microscopy (SEM) images were obtained

on a Hitachi F-4800 SEM (Hitachi, Ltd., Japan) equipped with an X-ray energy-dispersive spectrometer Oxford Leo Gemini 1530. Transmission electron microscope (TEM) observations were recorded on a JEOL-JEM 2100F TEM machine (Toray Research Center, Inc., Japan) operating at an acceleration voltage of 200 kV. The X-ray diffraction (XRD) measurements were conducted on a Philips X-Pert X-ray diffractometer (Rigaku Corporation, Japan) with a Cu Kα radiation source (λ=1.5418 Å). The Fourier transform infrared (FTIR) data were recorded on a Thermo Fisher Scientific's Nicolet 8700. The identical thermogravimetric analysis (TGA) measurements were carried out on a Mettler Toledo (heating rate of 10°C min^{-1}, from ambient temperature to 700°C). The X-ray photoelectron spectroscopy (XPS) was performed on a PHI Quantera-II SXM instrument (ULVAC-PHI, Japan) with Al Kα as the X-ray source. Time-resolved PL decay measurements were performed on an Edinburgh Instruments FLSP920 spectrometer using a time-correlated single-photon counting system with an excitation light from 320- and 405-nm laser diodes. Absolute PL QYs were measured on the same system equipped with an integrating sphere. The electron paramagnetic resonance (EPR) spectra were measured at room temperature on a JES FA200 spectrophotometer (X-band, 9.07 GHz; JEOL). ^{1}H nuclear magnetic resonance (NMR) and ^{13}C NMR results were both measured on a Bruker AV-400 spectrometer (Bruker, Ltd., Gemany). Raman spectra were collected on a high-resolution confocal RM2000 microscope spectrometer with a 532-nm laser as the excitation source.

3 Results and discussion

The chemical structure of the precursor $Al(acac)_3$ illustrated in Figure 1A demonstrates that central metal aluminum cation is surrounded by tridentate acetylacetone anions, revealing that the precursor provides aluminum, carbon, and oxygen elements, which are necessary for its emission [34, 35]. The main reason why we chose $Al(acac)_3$ as the precursor is that $Al(acac)_3$ exhibits a certain degree of crystallinity and good solubility in organic solvent such as toluene. Unit cell of $Al(acac)_3$

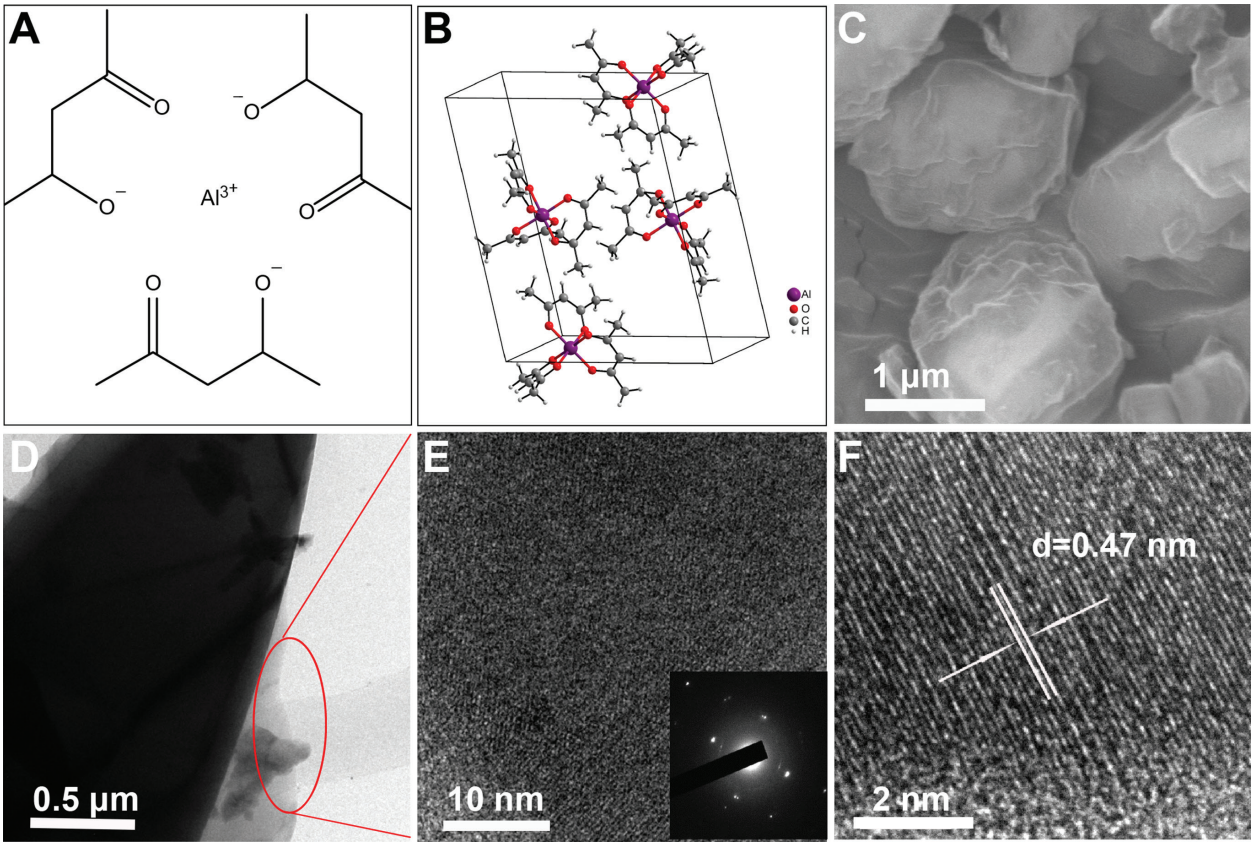

Figure 1: Structural and morphological characterization of $Al(acac)_3$ precursor and S1.
(A) Structural formula of $Al(acac)_3$ precursor. (B) Unit cell of $Al(acac)_3$ precursor crystals. (C) High-resolution SEM image of $Al(acac)_3$ precursor. (D) TEM image and (E) HRTEM image of lamellar structure of $Al(acac)_3$ precursor, the inset in the HRTEM image displays FFT pattern. (F) HRTEM image of S1 with lattice fringe of 0.47 nm.

crystal structure, as shown in Figure 1B, matches the monoclinic space group $P2_1/c$ with the following lattice parameters, $a = 13.985$ Å, $b = 7.54$ Å, and $c = 16.306$ Å [37]. We carried out SEM and TEM measurements to determine morphology of the precursor $Al(acac)_3$ crystals. Figure 1C provides a high-resolution SEM image, demonstrating a lamellar structure of each particle. Typical TEM image shown in Figure 1D further confirms the layered structure of the $Al(acac)_3$ crystals, in agreement with the SEM results. The high-resolution TEM (HRTEM) image (Figure 1E) provides enlarged lamella of thin edge region, presenting inconspicuous lattice fringes. The corresponding fast Fourier transform (FFT) pattern (inset of Figure 1E) points out the polycrystalline nature of $Al(acac)_3$ crystals. It is well known that thermal annealing process will increase the crystallization of materials [38]; thus, we performed thermal annealing of the precursor at 150°C under inert gas (N_2) to improve $Al(acac)_3$ crystallinity (the resulting sample after thermal annealing is denoted as S1). The HRTEM of S1 shown in Figure 1F reveals high quality of crystalline structure with lattice fringes of 0.47 nm, which confirms the crystallinity improvement due to thermal annealing.

The effortless fabrication process of $Al(acac)_3$ NCs is shown in Figure 2A, S1 powder was obtained through thermal annealing of $Al(acac)_3$ precursor and subsequently dissolved in toluene. The S1 solution underwent ultrasonic treatment to disintegrate the fragments aiming to form NCs. The experimental details are presented in the experimental section, and the obtained sample using this process is denoted as S2. The TEM measurements are performed to observe morphology and crystalline feature of S2, providing lots of NCs and a small number of lamellar structure (nondisintegrated precursor), as shown in Figure 2B–G. Figure 2B shows the low-resolution TEM image and size distribution of obtained NCs of S2. A large

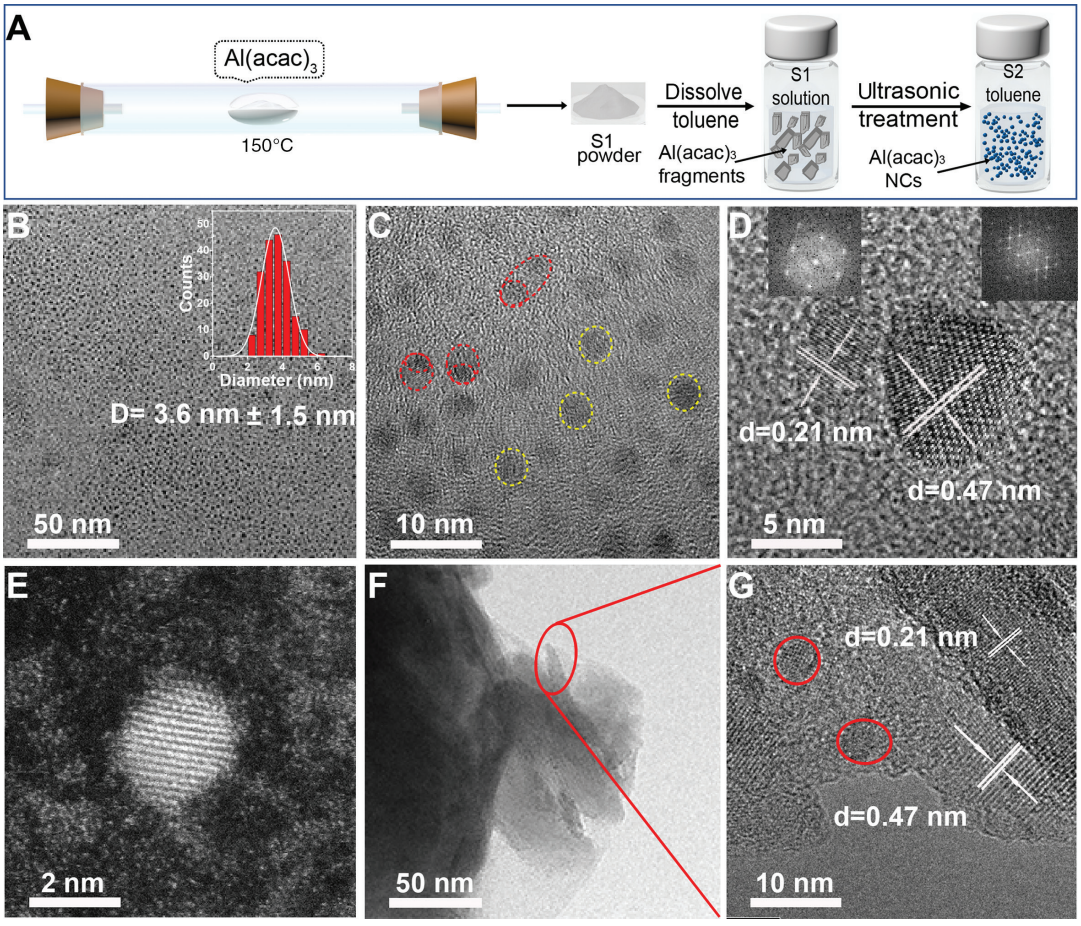

Figure 2: Schematic illustration of fabrication process and morphological characterization of S2.
(A) Schematic illustration for the fabrication of $Al(acac)_3$ NCs. (B) Low-resolution TEM image of monodispersed NCs of S2 and the corresponding size distribution of the NCs (inset). (C) HRTEM image of S2. (D) Enlarged HRTEM image to show Janus hybrid structure with two types of lattice fringes ($d = 0.21$ and 0.47 nm), and their FFT patterns are shown in inset. (E) The typical HAADF-STEM image of the single-type NCs with $d = 0.21$ nm. (F) TEM image of the existing nondisintegrated lamellar shape of S2 and corresponding enlarged HRTEM image (G).

area of nearly monodisperse colloidal nanocrystals (NCs) with a narrow size distribution of 3.6±1.5 nm is clearly observed, indicating that the precursor is disintegrated into nanosized crystals after sonication. Notably, there are two types of NCs, which can be obviously seen from HRTEM image (Figure 2C) elucidating the Janus-like NCs and mono-NCs indicated by red and yellow dashed ellipse, respectively. The enlarged HRTEM image (Figure 2D) along with FFT analysis provides one Janus-like NC with two different lattice fringes (d = 0.21 nm, d = 0.47 nm). The lattice spacing of 0.47 nm corresponds to the (211) crystal plane of $Al(acac)_3$, and the other lattice spacing of 0.21 nm is related to the (233) crystal plane of $Al(acac)_3$. Figure 2E demonstrates typical high-angle annular dark-field scanning TEM (HAADF-STEM) image of the other type of mono-NCs with d = 0.21 nm. It is worth noting that some NCs are embedded in the lamellar structure, which is marked by a red circle (Figure 2F, G), confirming that as-obtained monodispersed NCs of S2 arise from the precursor.

To confirm the phase structure of as-fabricated $Al(acac)_3$ NCs, we examined the XRD patterns of S2 and $Al(acac)_3$ precursor, as shown in Figure 3A, from which we can see that S2 retains the initial crystal structure of the precursor. The main peak positions at 2θ of 10.96°, 13.35°, 16.06°, 21.66°, and 23.83° match well with bulk monoclinic structure ($Al(acac)_3$; JCPDS no. 42-1746). The XRD results further indicate no other product obtained during thermal annealing and ultrasonic treatment of the precursor. X-ray diffraction pattern peaks of S2 narrow at 10.96°, 23.83°, and 13.35° compared with $Al(acac)_3$ precursor, indicating enhanced crystallinity of $Al(acac)_3$ NCs. To elucidate the chemical species of obtained $Al(acac)_3$ NCs, we performed FTIR spectra analysis as shown in Figure 3B. Clearly, the FTIR peaks and corresponding intensity of S2 are nearly the same as those of $Al(acac)_3$ precursor, suggesting unchanged chemical structure between product and precursor. The CH_2 and CH_3 stretching vibrations are observed in FTIR spectra between 2987 and 2931 cm^{-1}. The vibration absorption peaks from 1195 to 1580 cm^{-1} attributed to the asymmetric (ν_{as}) and symmetric (ν_s) stretching vibrations of $C\text{-}O^-$ and C=O, respectively [39]. The peaks located at 687 and 777 cm^{-1} in the FTIR spectra of S2 and precursor are ascribed to Al–O bond [40]. The same chemical structure behavior between our sample and the precursor is also verified by the Raman spectra (Figure S1) combined with NMR analysis involving ^1H NMR (Figure S2) and ^{13}C NMR (Figure S3), showing no shift of peaks and consistent related intensity of $Al(acac)_3$ NCs and $Al(acac)_3$ precursor. The distinct Raman peaks located at the range of 460–690 and 950–1372 cm^{-1} attribute to the stretching modes of the

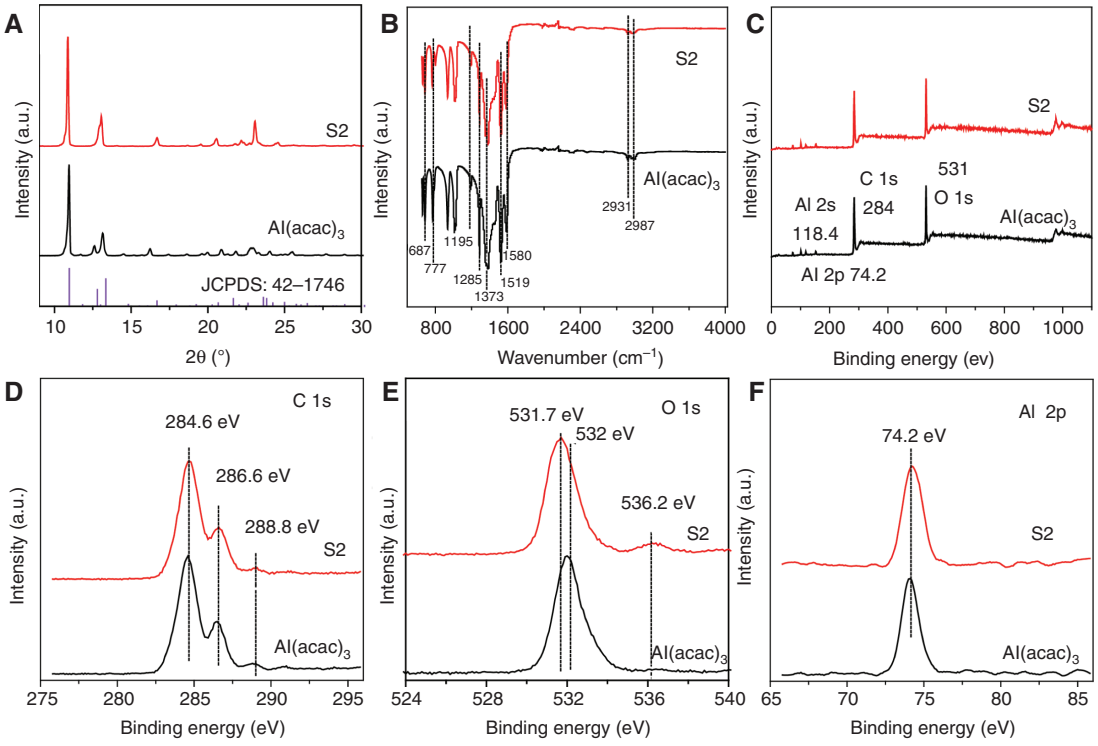

Figure 3: Structral characterization of S2.
(A) XRD patterns, (B) FTIR spectra, and (C) XPS survey spectra of S2 and $Al(acac)_3$ precursor. High-resolution XPS spectra of (D) C 1s, (E) O 1s, and (F) Al 2p.

Al–O and Al–O–C groups, respectively [41, 42]. The identical TGA curves of S2 and precursor (Figure S4) further support their consistent chemical structure. The XPS measurements are used to further investigate the surfaces of the samples. The survey XPS spectra presented in Figure 3C show four typical peaks: C 1s (284 eV), Al 2p (74.2 eV), Al 2s (118.4 eV), and O 1s (531 eV) [34]. In the high-resolution spectra (Figure 3D), the C 1s band contains three peaks, corresponding to sp^2 carbons (C=C, 284.6 eV), sp^3 carbons (C–O, 286.6 eV), and carbonyl carbons (C=O, 288.8 eV). The O 1s band contains two peaks at 531.7 and at 536.2 eV for C=O and C–O, respectively [43], as depicted in Figure 3E. The blue shift of the C=O peak position indicates that a slight change in the environment around the oxygen atom possibly related to partial Al–O band cleavage through ultrasonic process. The Al 2p XPS spectra (Figure 3F) show the same peak located at 74.2 eV, albeit differing in the full width at half maximum (1.3 eV for $Al(acac)_3$ precursor and 1.5 eV for S2), indicating a bit different chemical environment of Al element. Based on the above measurements analysis including XRD, Raman, FTIR, and XPS results, we can give the conclusion that no new chemical species formed after the precursor underwent thermal annealing and ultrasonic process; in other words, no decomposition reaction occurred during the experiment, but the precursor was pulverized into nanocrystalline particles.

The strong and stable emission features of NCs are essential for WLEDs. Absolute PL QY of S2 solution is measured to be 81.8% under excitation wavelength of 375 nm, the highest reported value for the aluminum compound-based NCs so far [36]. Unfortunately, the absolute PL QY of S2 powder sample is determined to be only 14.0% because of agglomeration of the NCs, which is a common aggregation-induced quenching phenomenon for other luminescent NCs [44]. S2 reveals very different optical properties compared with $Al(acac)_3$ precursor. Obviously, both precursor powder and dilute solution show extremely weak blue emission under 365-nm UV lamp irradiation, as shown in Figure 4A. The signal of blue emission of the precursor is difficultly detected by PL instrument. Thus, we obtain saturated solution of $Al(acac)_3$ precursor in toluene to measure the PL signal of the precursor. Figure S5 presents PL spectra of the high-concentration precursor solution, which confirms the presence of weak multiple peaks located at 409, 435, and 460 nm. Interestingly, S2 powder and solution samples exhibit bright blue emission under a 365-nm UV lamp, as shown in Figure 4B. The UV-vis absorption spectra (Figure 4C) show a significant difference between S2 and precursor, giving that precursor solution shows no absorption peak. But for S2 solution, peaks located at 355, 375, and 395 nm can obviously be observed, possibly attributed to exciton absorption from the quantum confinement effect of the S2 NCs. Furthermore, PL spectra (Figure 4D) measured at different excitation wavelengths ranging from 360 to 400 nm give the same three positions at 409, 435, and 460 nm, indicating that S2 has an excitation-independent PL feature. Remarkably, the PL peaks of S2 are completely consistent with those of high concentration of the precursor solution (Figure S5), which suggests that they have the same emission source. According to previous literatures [34, 35], the PL peak at 409 nm is attributed to lattice anion vacancies F^+ centers (oxygen vacancies occupied by one electron), whereas the PL peaks at 435 and 460 nm may arise from carbon-related defects. The PL excitation (PLE) spectra presented in Figure 4E show that S2 exhibits identical profile with three peaks at 355, 375, and 395 nm when changing the detection wavelength from 410 to 500 nm, substantially in agreement with the peaks of absorption spectra. We designed a control experiment to further illustrate the importance of simultaneous thermal annealing and ultrasonic treatment for high crystalline $Al(acac)_3$ NCs with high PL QYs. The control experiment was that the precursor underwent only ultrasonic treatment, but no annealing process, and the resulting sample was denoted as S3; the detailed results are shown in Figure S6, and the illustrations are given in the supporting information. And, other control experiments were conducted to monitor the effect of thermal annealing time of the precursor on PL QYs of $Al(acac)_3$ NCs. More results are given in Figure S7, and the corresponding explanations are provided in supporting information.

To illustrate the PL dynamics, the time-resolved PL decay curves (Figure 4F) collected at the emission peak of 460 nm under excitation wavelength ranging from 360 to 400 nm show identical profiles and monoexponential decay behavior with a lifetime of 0.9 ns. We employed the EPR technique to confirm the possible type of defects [45]. As shown in Figure 4G, the three samples of S1, S2, and $Al(acac)_3$ precursor exhibit the same EPR signal position with a *g* factor of 2.004, which further demonstrates that the emission source of S2 is the same as that of the S1 and $Al(acac)_3$ precursor. Previously, the *g* factor of 2.004 ascribed to radical carbonyl defects [34, 35]; thus, we can deduce that the emission peaks at 435 and 460 nm of our samples originate from radical carbonyl defects [46]. Furthermore, as shown in the inset of Figure 4G, S2 shows distinctly higher intensity of EPR signal than S1 and $Al(acac)_3$, which further verify that more radical carbonyl defects existed in NCs of S2 due to quantum confinement resulting in high PL QY. We further examined the stability

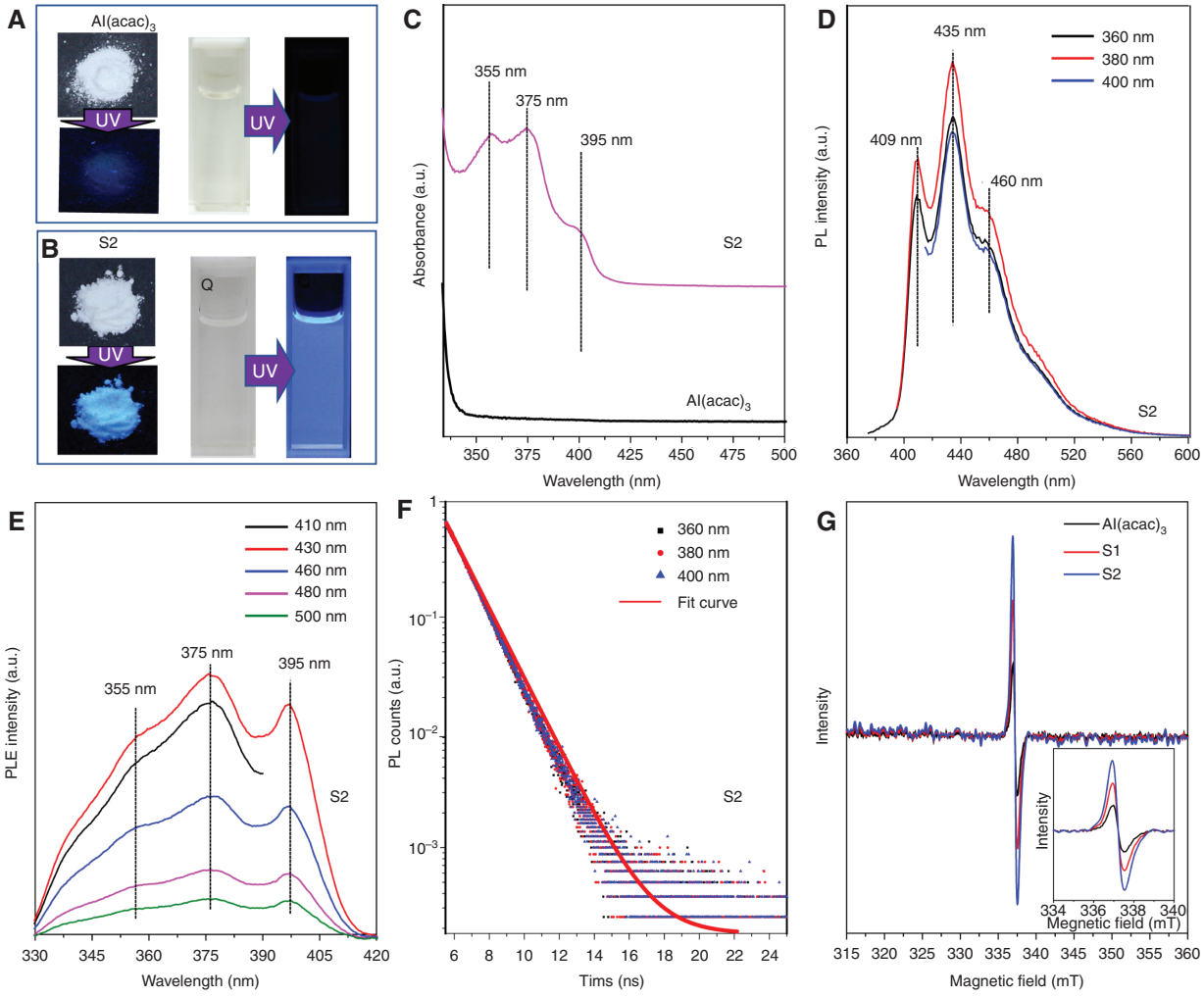

Figure 4: Optical properties of S2.
The photographs of (A) precursor and (B) sample (S2) under sunlight and 365-nm UV lamp as well as its corresponding (C) UV-vis absorption spectra. (D) PL spectra measured at different excitation wavelengths ranging from 360 to 400 nm. (E) PL excitation spectra monitored at different emission wavelengths from 410 to 500 nm. (F) Time-resolved PL decays and fitted curves of the light emission at 460 nm for S2 under different excitation wavelengths of 360, 380, and 400 nm. (G) X-band (9.07 GHz) EPR spectra of $Al(acac)_3$, S1, and S2, together with their enlarged-scale spectra given as an inset.

of S2 in an ambient atmosphere via detecting the variation of its PL QYs, which still maintain 61.2% of initial value after 1 year (detailed information in Table S1), indicating that S2 exhibits high stability against air.

The $Al(acac)_3$ NCs exhibit excellent solubility in toluene, which provides a good basis for solution-processed fabrication of composite film for remote UV-LED. The PMMA used as matrix to disperse NCs results in its strong emission; the function is the same as other polymer films [47]. We adopted the roller coating method to fabricate $Al(acac)_3$ NCs/PMMA composite film with a high PL QY of 40%. The three steps of the process are as shown in Figure 5A. In Stage I, the $Al(acac)_3$ NC solution and the PMMA solution were stirred and mixed (specific experimental details in the experimental part); the mixture solution was dropped on a glass substrate with a pipette. In Stage II, the film was flattened with a glass rod. In Stage III, the wet film was placed in a ventilated place to naturally evaporate the solvent to obtain a transparent film.

As illustrated in Figure 5B, the pristine $Al(acac)_3$ NCs/PMMA composite film appears smooth and transparent in air exposure, which is correlated with high transmission rate (>88%) as displayed in Figure 5C. The PLE spectrum (Figure 5D) of the composite film shows three typical peaks at 355, 377, and 395 nm, in agreement with that of $Al(acac)_3$ NC solution in toluene, indicating that $Al(acac)_3$ NCs are successfully embedded in the PMMA matrix. The blue emission behavior (inset of Figure 5E) of the composite film further confirms the insertion of $Al(acac)_3$ NCs in PMMA. Figure 5E provides

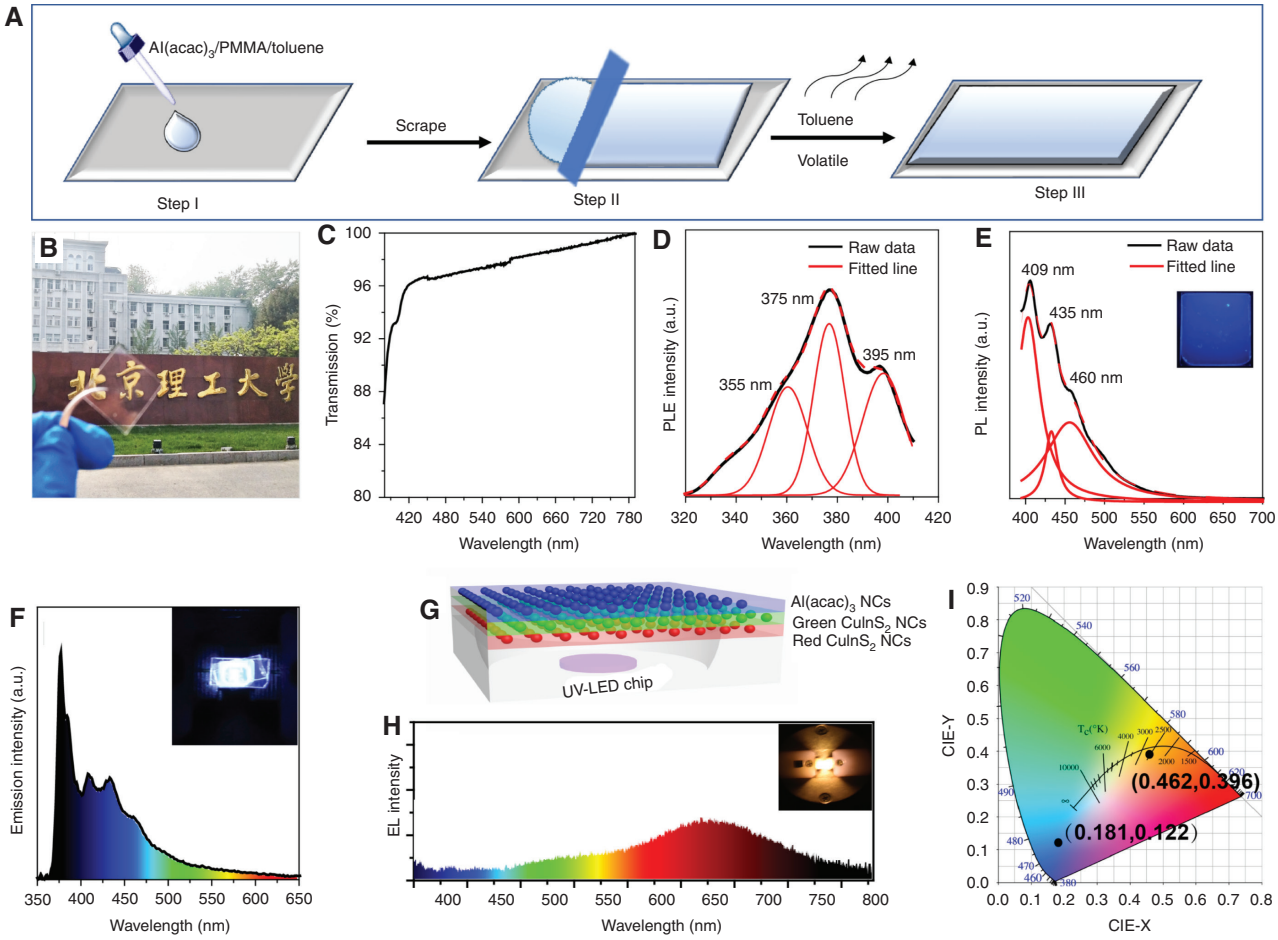

Figure 5: Fabrication process and optical characterization of Al(acac)$_3$ NCs/PMMA film, and the performance of LED devices. (A) Schematic illustration of the fabrication of Al(acac)$_3$ NCs embedded PMMA composite film. (B) The optical image of Al(acac)$_3$ NCs/PMMA composite film with a size of 2 × 2 cm under ambient day light. (C) Transmission spectrum of the composite film. (D) PLE spectrum under emission peak at 430 nm. (E) PL spectrum under excitation wavelength of 395 nm; inset shows the photograph of composite film under 365-nm UV lamp. (F) Emission spectrum of as-obtained remote UV-LED device by using single Al(acac)$_3$ NCs/PMMA composite film, inset: blue emission photograph of operating LED device. (G) Schematic diagram of remote UV-WLED–based three color films of blue-emitting Al(acac)$_3$/PMMA, green-emitting, and red-emitting CuInS$_2$/PMMA. (H) Emission spectrum of the operating remote UV-WLED with corresponding photograph shown in inset. (I) CIE chromaticity diagram of remote blue LED and UV-WLED devices.

PL spectrum examined at excitation wavelength of 395 nm. Three distinctive peaks at 409, 435, and 460 nm are consistent with the initial Al(acac)$_3$ NC solution sample. It is noteworthy that the enhanced intensity of peak at 409 nm is observed compared with that at 435 and 460 nm. The possible reason is that PMMA can provide carbon matrix, which leads to reduced carbon-related defects of Al(acac)$_3$ NCs; thus, the PL intensities of 435 and 460 nm are significantly reduced compared with 409 nm.

To explore the use of Al(acac)$_3$ NCs/PMMA composite film in LED device, we first fabricated monochromatic remote UV-LED. Figure 5F shows emission spectrum of the blue-emitting LED, which provides four emission peaks. The peak at 370 nm arises from the UV-LED chip, and other peaks at 409, 435, and 460 nm originate from the Al(acac)$_3$ NCs, consistent with their PL spectra (Figure 4E). The Commission Internationale de L'Eclairage (CIE) color coordinates of LED operated at a forward bias current of 20 mA, (0.181, 0.122) are marked in CIE 1931 chromaticity diagram (Figure 5I). To demonstrate the ability of blue-emitting composite film to generate high-quality white light, we fabricated remote UV-WLEDs by combining Al(acac)$_3$ NCs/PMMA with red-emissive and green-emissive CuInS$_2$ NCs/PMMA composite films (PL spectra shown in Figure S8). The remote configuration of the device is shown in Figure 5G, providing a UV-LED chip with 370 nm as the excitation source. Figure 5H shows warm white-light emission of the WLED operated under a 20-mA drive current. The emission spectrum (Figure 5H) reveals

three color regions; blue emission peaks at 409, 435, and 465 nm due to the $Al(acac)_3$ NCs/PMMA composite film. Green emission peak at 520 nm arises from green-emitting $CuInS_2$ composite film, and red color of 675 nm derives from the red-emitting $CuInS_2$ composite film. The as-fabricated remote UV-WLEDs achieve a high CRI of 91. The CIE color coordinate of the WLED with color-correlated temperature (CCT) of 2553 K is (0.462, 0.396), which is marked in CIE 1931 color space, and the color points approach the black body Planckian locus (Figure 5I), indicating that the remote UV-WLEDs produce a high-quality lighting. Furthermore, we use a direct laser writing technology to fabricate a patterned $Al(acac)_3$ NCs/PMMA composite film with a logo of Beijing Institute of Technology (BIT) (Figure S9A), which shows bright blue emission under 365-nm UV lamp excitation (Figure S9B), suggesting that it could be a potential candidate for display application.

4 Conclusions

In summary, we demonstrated a facile top-down approach to fabricate blue-emissive $Al(acac)_3$ NCs by using crystalline $Al(acac)_3$ as a precursor. The fabrication process could be divided into two steps including thermal annealing and ultrasonic treatment. The as-obtained final product exhibited multiple PL peaks behavior arising from F^+ centers and carbon-related defects with high PL QY of 81.8% related to quantum confinement of $Al(acac)_3$ NCs. Moreover, blue-emissive $Al(acac)_3$ NCs /PMMA composite film was fabricated by using a simple roller coating method for UV-pumped LED. We combined a blue-emitting $Al(acac)_3$ NCs/PMMA composite film with red- and green-emitting $CuInS_2$ NCs/PMMA films to achieve warm white-light remote UV-WLEDs with a high CRI value of 91 and CCT of 2553 K. We believe that the resulting $Al(acac)_3$ NCs can grow as a new type of NCs for potential optoelectronic applications such as lighting, displays, lasers, and photodetectors.

Acknowledgments: This work was supported by the Natural Science Foundation of Youth Fund Project of China (No. 51602024), National Key Research and Development Program of China (No. 2016YFB0401202), Beijing Nova Program (No. Z171100001117047), National Natural Science Foundation of China (No. 61727808, 61661146002, 61775019, Funder Id: http://dx.doi.org/10.13039/501100001809), and Beijing Outstanding Young Scientist Program (BJJWZYJH01201910007022). The authors thank Prof. Haizheng Zhong (School of Materials Science & Engineering, BIT) for his support of optical measurements.

References

[1] Schubert EF, Kim JK. Solid-state light sources getting smart. Science 2005;308:1274–8.
[2] Chen L, Lin C-C, Yeh C-W, Liu R-S. Light converting inorganic phosphors for white light-emitting diodes. Materials 2010;3:2172–95.
[3] Ye S, Xiao F, Pan YX, Ma YY, Zhang QY. Phosphors in phosphor-converted white light-emitting diodes recent advances in materials, techniques and properties. Mater Sci Eng R-Rep 2010;71:1–34.
[4] Li GG, Tian Y, Zhao Y, Lin J. Recent progress in luminescence tuning of Ce^{3+} and Eu^{2+}–activated phosphors for pc-WLEDs. Chem Soc Rev 2015;44:8688–713.
[5] Wang L, Xie R-J, Suehiro T, Takeda T, Hirosaki N. Down-conversion nitride materials for solid state lighting: recent advances and perspectives. Chem Rev 2018;118:1951–2009.
[6] Shang Y-M, Wang G-S, Sliney D, Yang C-H, Lee L-L. White light-emitting diodes (LEDs) at domestic lighting levels and retinal injury in a rat model. Environ Health Perspect 2014;122:269–76.
[7] Kim YH, Viswanath NSM, Unithrattil S, Kim HJ, Im WB. Review-phosphor plates for high-power LED applications: challenges and opportunities toward perfect lighting. ECS J Solid State Sci Technol 2018;7:R3134–47.
[8] Le T-H, Choi Y, Han H, et al. Highly luminescent quantum dots in remote-type liquid-phase color converters for white light-emitting diodes. Adv Mater Technol 2018;3:1800235.
[9] Sun C, Zhang Y, Ruan C, et al. Efficient and stable white LEDs with silica-coated inorganic perovskite quantum dots. Adv Mater 2016;28:10088–94.
[10] Erdem T, Demir HV. Color science of nanocrystal quantum dots for lighting and displays. Nanophotonics 2013;2:57–81.
[11] Shirasaki Y, Supran GJ, Bawendi MG, Bulovic V. Emergence of colloidal quantum-dot light-emitting technologies. Nat Photonics 2013;7:13–23.
[12] Fu M, Ehrat F, Wang Y, et al. Carbon dots: a unique fluorescent cocktail of polycyclic aromatic hydrocarbons. Nano Lett 2015;15:6030–5.
[13] Leng MY, Chen ZW, Yang Y, et al. Lead-free, blue emitting bismuth halide perovskite quantum dots. Angew Chem Int Edit 2016;55:15012–6.
[14] Jing LH, Kershaw SV, Li YL, et al. Aqueous based semiconductor nanocrystals. Chem Rev 2016;116:10623–730.
[15] Dabbousi BO, Rodriguez-Viejo J, Mikulec FV, et al. (CdSe)ZnS core-shell quantum dots: synthesis and characterization of a size series of highly luminescent nanocrystallites. J Phys Chem B 1997;101:9463–75.
[16] Gerion D, Pinaud F, Williams SC, et al. Synthesis and properties of biocompatible water-soluble silica-coated CdSe/ZnS semiconductor quantum dots. J Phys Chem B 2001;105:8861–71.
[17] Qu LH, Yu WW, Peng XG. In situ observation of the nucleation and growth of CdSe nanocrystals. Nano Lett 2004;4:465–9.
[18] Bae WK, Lim J, Lee DG, et al. R/G/B/Natural white light thin colloidal quantum dot-based light-emitting devices. Adv Mater 2014;26:6387–93.
[19] Xie RG, Peng XG. Synthesis of Cu-doped InP nanocrystals (d-dots) with ZnSe diffusion barrier as efficient and color-tunable NIR emitters. J Am Chem Soc 2009;131:10645–51.
[20] Huang F, Bi CH, Guo RQ, Zheng C, Ning JJ, Tian JJ. Synthesis of colloidal blue-emitting InP/ZnS core/shell quantum dots with the assistance of copper cations. J Phys Chem Lett 2019;10:6720–6.

[21] Zhang F, Zhong HZ, Chen C, et al. Brightly luminescent and color-tunable colloidal $CH_3NH_3PbX_3$ (X=Br, I, Cl) quantum dots: potential alternatives for display technology. ACS Nano 2015;9:4533–42.
[22] Akkerman QA, Raino G, Kovalenko MV, Manna L. Genesis, challenges and opportunities for colloidal lead halide perovskite nanocrystals. Nat Mater 2018;17:394–405.
[23] Chang S, Bai ZL, Zhong HZ. In situ fabricated perovskite nanocrystals: a revolution in optical materials. Adv Opt Mater 2018;6:1800380.
[24] Wang L, Meng LH, Chen L, et al. Ultralow-threshold and color-tunable continuous-wave lasing at room-temperature from in situ fabricated perovskite quantum dots. J Phys Chem Lett 2019;10:3248–53.
[25] Fang MJ, Huang SH, Li D, et al. Stretchable and self-healable organometal halide perovskite nanocrystal–embedded polymer gels with enhanced luminescence stability. Nanophotonics 2018;7:1949–58.
[26] Sun C, Gao ZY, Liu HX, et al. One stone, two birds: high-efficiency blue-emitting perovskite nanocrystals for LED and security ink applications. Chem Mater 2019;31:5116–23.
[27] Sun C, Su SJ, Gao ZY, et al. Stimuli-responsive inks based on perovskite quantum dots for advanced full-color information encryption and decryption. ACS Appl Mater Interfaces 2019;11:8210–6.
[28] Wang HG, Wang ZG, Xiong Y, et al. Hydrogen peroxide assisted synthesis of highly luminescent sulfur quantum dots. Angew Chem-Int Edit 2019;58:7040–4.
[29] Cheng XY, Lowe SB, Reece PJ, Gooding JJ. Colloidal silicon quantum dots: from preparation to the modification of self-assembled monolayers (SAMs) for bio-applications. Chem Soc Rev 2014;43:2680–700.
[30] Yuan FL, Yuan T, Sui LZ, et al. Engineering triangular carbon quantum dots with unprecedented narrow bandwidth emission for multicolored LEDs. Nat Commun 2018;9:2249.
[31] Chen S, Cao WR, Liu TL, et al. On the degradation mechanisms of quantum-dot light-emitting diodes. Nat Commun 2019;10:765.
[32] Moon H, Lee C, Lee W, Kim J, Chae H. Stability of quantum dots, quantum dot films, and quantum dot light-emitting diodes for display applications. Adv Mater 2019;31:1804294.
[33] Bai X, Caputo G, Hao ZD, et al. Efficient and tuneable photoluminescent boehmite hybrid nanoplates lacking metal activator centres for single-phase white LEDs. Nat Commun 2014;5:5702.
[34] Chen BK, Susha AS, Reckmeier CJ, et al. Mesoporous aluminum hydroxide synthesized by a single-source precursor-decomposition approach as a high-quantum-yield blue phosphor for UV-pumped white-light–emitting diodes. Adv Mater 2017;29:1604284.
[35] Chen BK, Xu XJ, Zou SY, et al. Single source precursor chemical vapor decomposition method to fabricate stable, bright emissive aluminum hydroxide phosphors for UV-pumped white light-emitting devices. Adv Opt Mater 2018;6:1701115.
[36] Li TH, Liu LZ, Wu XL, Shen JC, Gao F, Chu PK. Photoluminescence from colloids containing aluminum hydroxide nanocrystals with uniform size. Appl Phys Lett 2010;97:121901.
[37] Bott SG, Fahlman BD, Pierson ML, Barron AR. An accuracy assessment of the refinement of partial metal disorder in solid solutions of $Al(acac)_3$ and $Cr(acac)_3$. J Chem Soc Dalton Trans 2001;2148–52.
[38] Gao K, Jo SB, Shi XL, et al. Over 12% efficiency nonfullerene all-small-molecule organic solar cells with sequentially evolved multilength scale morphologies. Adv Mater 2019;31:1807842.
[39] Damm H, Kelchtermans A, Bertha A, et al. Thermal decomposition synthesis of Al-doped ZnO nanoparticles: an in-depth study. RSC Adv 2013;3:23745–54.
[40] Gangwar J, Gupta BK, Tripathi SK, Srivastava AK. Phase dependent thermal and spectroscopic responses of Al_2O_3 nanostructures with different morphogenesis. Nanoscale 2015;7:13313–44.
[41] Ruan HD, Frost RL, Kloprogge JT. Comparison of Raman spectra in characterizing gibbsite, bayerite, diaspore and boehmite. J Raman Spectrosc 2001;32:745–50.
[42] Reyes-Lopez SY, Acuna RS, Lopez-Juarez R, Rodriguez JS. Analysis of the phase transformation of aluminum formate $Al(O_2CH)_3$ to α-alumina by Raman and infrared spectroscopy. J Ceram Process Res 2013;14:627–31.
[43] Ding H, Yu SB, Wei J-S, Xiong HM. Full-color light-emitting carbon dots with a surface-state–controlled luminescence mechanism. ACS Nano 2016;10:484–91.
[44] Zhou D, Di L, Jing PT, et al. Conquering aggregation-induced solid-state luminescence quenching of carbon dots through a carbon dots-triggered silica gelation process. Chem Mater 2017;29:1779–87.
[45] Wakui Y, Takahashi K, Shan YJ, et al. Study on effects of carbon impurities and oxygen vacancies in amorphous alumina phosphor prepared via a solution method. J Lumines 2015;157:137–42.
[46] Lin CK, Yu M, Cheng ZY, Zhang CM, Meng OG, Lin J. Bluish-white emission from radical carbonyl impurities in amorphous Al_2O_3 prepared via the Pechini-type sol–gel process. Inorg Chem 2008;47:49–55.
[47] Li XM, Wu Y, Zhang SL, et al. $CsPbX_3$ quantum dots for lighting and displays: room-temperature synthesis, photoluminescence superiorities, underlying origins and white light-emitting diodes. Adv Funct Mater 2016;26:2435–45.

Supplementary Material: The online version of this article offers supplementary material (https://doi.org/10.1515/nanoph-2020-0142).